Catalysis Science & Technology

PAPER

View Article Online
View Journal | View Issue

Cite this: *Catal. Sci. Technol.*, 2016, **6**, 7231

Oxygen reduction reaction at $La_xCa_{1-x}MnO_3$ nanostructures: interplay between A-site segregation and B-site valency†

Verónica Celorrio,[a] Laura Calvillo,[b] Ellie Dann,[a] Gaetano Granozzi,[b] Ainara Aguadero,[c] Denis Kramer,[d] Andrea E. Russell[e] and David J. Fermín*[a]

Received 20th May 2016,
Accepted 13th July 2016

DOI: 10.1039/c6cy01105e

www.rsc.org/catalysis

The mean activity of surface Mn sites at $La_xCa_{1-x}MnO_3$ nanostructures towards the oxygen reduction reaction (ORR) in alkaline solution is assessed as a function of the oxide composition. Highly active oxide nanoparticles were synthesised by an ionic liquid-based route, yielding phase-pure nanoparticles, across the entire range of compositions, with sizes between 20 and 35 nm. The bulk *vs.* surface composition and structure are investigated by X-ray diffraction (XRD), X-ray photoelectron spectroscopy (XPS) and X-ray absorption near edge spectroscopy (XANES). These techniques allow quantification of not only changes in the mean oxidation state of Mn as a function of *x*, but also the extent of A-site surface segregation. Both trends manifest themselves in the electrochemical responses associated with surface Mn sites in 0.1 M KOH solution. The characteristic redox signatures of Mn sites are used to estimate their effective surface number density. This parameter allows comparing, for the first time, the mean electrocatalytic activity of surface Mn sites as a function of the $La_xCa_{1-x}MnO_3$ composition. The ensemble of experimental data provides a consistent picture in which increasing electron density at the Mn sites leads to an increase in the ORR activity. We also demonstrate that normalisation of electrochemical activity by mass or specific surface area may result in inaccurate structure–activity correlations.

1. Introduction

The development of non-noble metal catalysts for oxygen reduction (ORR) and evolution reactions is one of the greatest challenges in the field of energy conversion, from fuel cells to Li–air batteries.[1–4] Transition metal oxides, such as perovskites, have been reported as active materials for ORR in alkaline media,[4–6] although the identification of suitable activity descriptors for this vast family of materials remains controversial.[7–10] In the specific case of perovskites, ABO_3, the electrocatalytic activity has been linked to the nature and coordination of the B-site, as well as the overall number of electrons in d-orbitals and electron occupancy of e_g orbitals at the B-site.[11–16] These parameters are strongly correlated with the nature of the A-site as well as oxygen vacancies. The role of carbon supports, often employed in order to improve charge transport to the oxide particles, also requires careful consideration given the fact that oxygen can be reduced at the carbon layer in alkaline solutions.[17] All of these variables, in addition to other more obvious parameters such as average particle size and phase purity, make the establishment of structure–activity relationships extremely challenging.

$LaMnO_{3+\delta}$ has been reported as one of the most active perovskite materials for the ORR.[7,16,18] A growing number of publications on the electrocatalytic properties of Mn-based oxides have emerged in recent years,[19–24] proposing composition–activity relationships which may appear somewhat contradictive. For instance, Stoerzinger *et al.* concluded that Mn^{3+} sites are the most active for ORR in $La_{1-x}(Ca, Sr)_xMnO_3$ (011)-oriented films.[24] In a subsequent work, it is proposed that the most active composition of $La_{(1-x)}Sr_xMnO_3$ contains 33% Sr, promoting a mixed $Mn^{3+/4+}$ state.[23] Du *et al.* also concluded that a mixed valency of $Mn^{3+/4+}$ is the most active in $CaMnO_{3-\delta}$ with $0 < \delta < 0.5$.[25] The interesting review by Stoerzinger *et al.* shows a significant spread in the activity of Mn oxide catalysts, based on kinetic current normalized by mass at a given potential, spanning by several orders of magnitude.[18]

[a] *School of Chemistry, University of Bristol, Cantocks Close, BS8 1TS, Bristol, UK. E-mail: David.Fermin@bristol.ac.uk*
[b] *Dipartimento di Scienze Chimiche, Università di Padova, Via Marzolo 1, 35131 Padova, Italy*
[c] *Department of Materials, Imperial College, SW7 2AZ, London, UK*
[d] *Engineering Sciences, University of Southampton, SO17 1BJ, Southampton, UK*
[e] *Chemistry, University of Southampton, SO17 1BJ, Southampton, UK*

† Electronic supplementary information (ESI) available: TEM images, particle size distributions, H-Res TEM images, Mn $2p_{3/2}$ inset, XANES spectra for standard Mn compounds, calculation of the number of Mn sites, cyclic voltammetry in Ar-saturated solution, RRDE data for $CaMnO_3$ at different rotation rates, calculation of the number of electrons and HO_2^- yield, Koutecky–Levich plots and different normalizations for i_k. See DOI: 10.1039/c6cy01105e

The complexity of these systems arises not only from bulk structural properties such as phase purity, but also from off-stoichiometric surface composition due to preferential elemental segregation.[12,26] For instance, Lee *et al.* showed that the tendency of $La_xA_{1-x}MnO_3$ to segregate is dependent on the size between the host and the dopant following the trend Ba > Sr > Ca.[12] Consequently, it is a real challenge to estimate the electroactive surface area of these materials not only in the case of nanoparticles supported on porous carbon layers, but also in continuous thin films.

This work assesses, for the first time, the mean activity of individual surface Mn-sites in a family of $La_xCa_{1-x}MnO_3$ nanoparticles towards the ORR in alkaline solutions. Oxide nanoparticles across the entire composition range were synthesised with a high degree of phase purity employing an ionic liquid-based approach.[16] Quantitative analysis based on X-ray diffraction, X-ray photoemission spectroscopy and X-ray absorption near edge spectroscopy allowed uncovering of the bulk and surface structures of the oxide nanostructures, as well as the mean Mn oxidation state. Kinetic current values normalised by either the mass or specific surface area of the catalysts showed that these materials rank among the most active for the ORR, although the composition dependence is somewhat unclear employing these standard normalisation parameters. However, a clearer trend emerges when the kinetic responses are normalised by the mean Mn surface number density obtained from electrochemical analysis. We conclude that the activity of surface Mn sites increases as the mean oxidation state decreases promoted by increasing La content on the A-site.

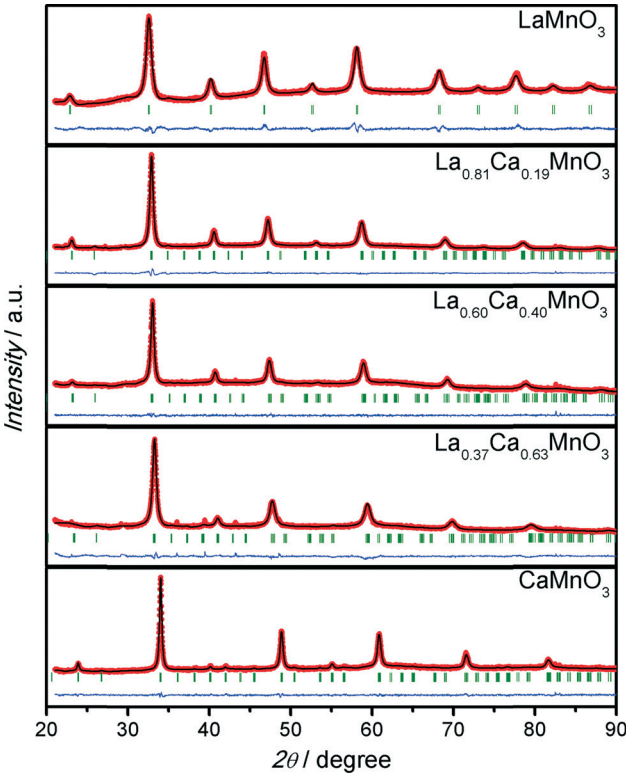

Fig. 1 XRD patterns of $LaMnO_3$, $La_{0.81}Ca_{0.19}MnO_3$, $La_{0.60}Ca_{0.40}MnO_3$, $La_{0.37}Ca_{0.63}MnO_3$ and $CaMnO_3$. Red dots correspond to the experimental values while the black thin line corresponds to the Rietveld refinement. The thin blue line shows the difference between the experimental and refined patterns. The green bars correspond to the positions of the allowed Bragg reflections for the main phase.

2. Results and discussion

Highly crystalline and phase-pure $La_xCa_{1-x}MnO_3$ nanoparticles are obtained by calcination of the ionic liquid-based precursors across the whole range of compositions as demonstrated by the XRD patterns shown in Fig. 1. Transmission electron microscopy (TEM) images show faceted nanoparticles featuring a relatively narrow size dispersion, no porosity and relatively narrow size distributions with mean particle sizes between 26 and 32 nm (Fig. S1 and S2†). Lattice fringes with different spacings can be observed in the high-resolution TEM images (Fig. S3†), which further demonstrate the highly polycrystalline nature of the samples. Rietveld refinements of the XRD patterns in Fig. 1 demonstrate not only strong agreement with the identified primary phase, but also the absence of secondary phases. The incorporation of Ca into the A-site leads to a shift in the peaks towards higher 2θ angles, which can be clearly seen in the peak centred at 32°. This shift is a consequence of the strain introduced by the smaller Ca^{2+} cation (0.134 nm) compared to La^{3+} (0.136 nm).[22,27] Parameters such as the replacement of Mn^{3+} ions (atomic radii 0.645 Å) by Mn^{4+} (atomic radii 0.53 Å) ions and the presence of oxygen vacancies also affect the lattice constants.

The crystal structure of $LaMnO_3$ was accurately refined in the cubic *Pm*3*m* space group without the need for any added structural distortion. Every feature in the XRD pattern was accurately refined justifying the assignment of the most symmetrical group. However, it is important to note that the relatively broad XRD features arising from the small particle sizes may introduce a degree of uncertainty in the identification of the $LaMnO_3$ phase group, which has been previously assigned to the orthorhombic *Pbnm* phase at room temperature.[28] On the other hand, $CaMnO_3$ and the mixed compositions $La_xCa_{1-x}MnO_3$ were accurately refined in the orthorhombic *Pnma* space group. Table S1† summarizes the unit-cell parameters and discrepancy factors after the refinements. It could be seen that the unit cell volume shows a non-monotonic dependence on the La content due to the influence of a variety of parameters such as contrast in ionic radii, the oxidation state of Mn and the presence of oxygen vacancies. Table S2† shows the atomic composition of the materials as obtained by SEM-EDX, which closely reflects the composition of the ionic liquid precursor. Table S3† outlines the corresponding specific surface area (SSA) estimated for the various oxide nanostructures. In view of the relatively narrow size distribution and low porosity of the nanoparticles, the SSA was estimated employing a geometric approximation and the material density which was obtained from the XRD refinement analysis.

Core level photoemission spectra of La 3d, Ca 2p, O 1s and Mn 2p regions for the various $La_xCa_{1-x}MnO_3$ samples are displayed in Fig. 2. The La 3d lines (Fig. 2a) show typical double splitting due to the spin–orbit interaction and the shake-up excitation of an oxygen valence band electron to the empty La 4f level. The La $3d_{5/2}$ is located at 834.4 eV, corresponding to La^{3+} compounds,[29,30] and does not change with the addition of Ca.

The Ca 2p photoemission line can be deconvoluted into two components (Fig. 2b and Table S4†). Ca^{2+} at the perovskite lattice exhibits a binding energy (BE) shift from 344.8 eV to 346.3 eV with increasing La content. This shift has already been observed in the literature but no clear explanation has been reported.[29,31] In principle, this effect can be attributed to the changes in the nearest neighbors of Ca atoms: the variation of the amount of La is expected to change the electronic structure of the oxygens and consequently that of the Ca atoms. The second Ca $2p_{3/2}$ component identified in the range of 346.7–347.4 eV is attributed to the formation of $CaCO_3$ and/or CaO at the oxide surface due to Ca segregation.[20,32] The presence of a C 1s component at 289.6 eV (Fig. S4a†) and O 1s at 532.2 eV is consistent with the generation of $CaCO_3$ and CaO at the oxide surface.

The O 1s photoemission peak is deconvoluted into five contributions described by symmetrical Voigt functions (see Fig. 2c and Table S5†). The lower BE component is assigned to oxygen in the perovskite lattice (metal–oxygen bonds) centred at 528.5 eV.[33] In the case of the samples containing La, this component becomes very small due to the segregation of La and consequent formation of La_2O_3 at the surface. The presence of the La_2O_3 species is represented by the component at 529.3 eV. The third component at 530.9–531.1 eV is attributed to hydroxyl groups, whereas that at about 532.1 eV can be associated with CaO and/or $CaCO_3$ formed at the surface due to Ca segregation, as well as with carbonyl groups. The component at higher BE is associated with adsorbed water.[20,30,34]

The photoemission lines in the Mn 2p region are displayed in Fig. 2d, with the Mn $2p_{3/2}$ peak located at 642 eV. This broad peak contains the contribution from Mn^{3+} (641.9 eV) and Mn^{4+} (642.2 eV) signals.[29] The maximum BE value of this signal shifts towards lower energies as x increases (see also Fig. S4†), which is consistent with an

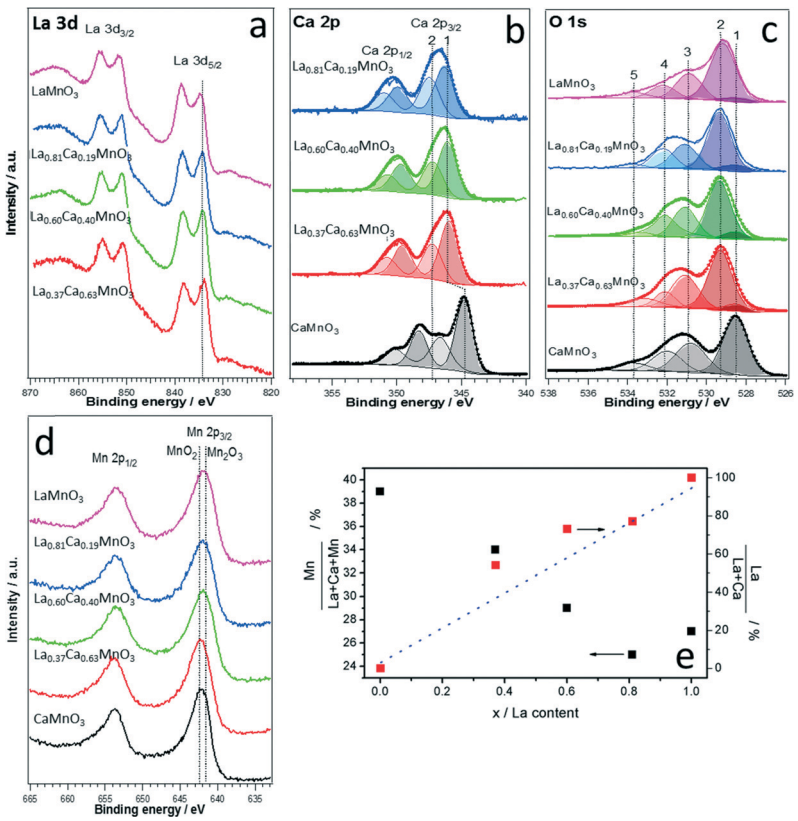

Fig. 2 La 3d (a), Ca 2p (b), O 1s (c) and Mn 2p (d) photoemission spectra of the various $La_xCa_{1-x}MnO_3$ oxides taken in normal emission using a non-monochromatic Al Kα X-ray source. Two main contributions to the Ca 2p region were identified: Ca in the lattice (1) and surface CaO/$CaCO_3$ (2). The peaks in the O 1s region were assigned to lattice oxygen (1), La_2O_3 species (2), surface hydroxyl species (3), carbonyl groups and CaO/$CaCO_3$ groups (4), and adsorbed molecular water (5). Figure (e) shows the evolution of the surface atomic ratio of the A- and B-sites as a function of the La content x. Red squares correspond to the ratio of La/(La + Ca), which deviates from the bulk value represented by the blue dotted line at intermediate x values. Black squares show the ratio of B/(A + B) sites. According to the bulk composition, this value should be close to 50%. However, data show the substantial depletion of the B-sites upon increasing the La content.

increase in the Mn^{3+}/Mn^{4+} ratio. Quantitative deconvolution of the two Mn oxidation states is rather challenging given the small differences in BE values. As discussed below, XANES analysis provides a far more accurate determination of the mean Mn oxidation state.

The surface composition of $La_xCa_{1-x}MnO_3$ obtained from the photoemission studies is summarised in Fig. 2e (see also Table S6†). Due to the polycrystalline nature of the samples, the surface composition can only be considered as an effective value rather than a specific facet of the nanoparticles. The first interesting observation is that the surface atomic ratio of La and Ca is different from the bulk ratio (dotted line). For x values between 0.4 and 0.6, the surface La content is higher than that in the bulk, demonstrating the preferential segregation of this cation, which forms La_2O_3 at the surface. It is also observed that the atomic ratio of A- to B-sites significantly deviates from the bulk values as the La content increases. A-site segregation has been consistently observed in perovskite materials prepared at high temperature.[13,35,36] However, the A-site surface segregation trend seems to break down at high x-values in $La_xCa_{1-x}MnO_3$, with $LaMnO_3$ showing a higher surface Mn content than $La_{0.81}Ca_{0.19}MnO_3$. As demonstrated further below, this trend is also consistent with electrochemical responses sensitive to the surface density of Mn sites.

The mean oxidation state of Mn sites as a function of the perovskite composition is estimated from the XANES spectra displayed in Fig. 3a. The main Mn K-edge in the case of $LaMnO_3$ is shifted by 4 eV to lower energies in comparison to $CaMnO_3$. A similar difference is observed between MnO_2 and Mn_2O_3 standards (Fig. S5†), which is consistent with Mn^{3+} and Mn^{4+} oxidation states.[37,38] The inset in Fig. 3a shows that the intensity of the pre-edge feature decreases with increasing La content, further confirming a decrease in the mean Mn oxidation state with increasing La content.[37,39]

The Mn K-edge position can also be affected by local distortion of the MnO_6 octahedra, leading to an apparent edge shift even in the absence of an oxidation state change.[40–42] Consequently, the Mn valency was probed from the pre-edge energy position following the approach reported by Croft *et al.*[43] Fig. 3b shows a linear relationship between the pre-edge position (established from the first derivative of the spectra) and the Mn oxidation state of the standards MnO_2, Mn_2O_3 and Mn_3O_4, in agreement with literature values.[39,43] The mean Mn oxidation state of $La_xCa_{1-x}MnO_3$ was estimated from the trend shown in Fig. 3b, providing values consistent with the composition of the A-site. For instance, the pre-edge position of $CaMnO_3$ was very close to that of the standard MnO_2, confirming the predominance of a Mn^{4+} oxidation state. It can also be seen that increasing values of x lead to a decrease in the mean Mn oxidation state. It is interesting to note that Mn exhibits a 2.8 oxidation state in the case of $LaMnO_3$, strongly indicating the presence of oxygen vacancies.

Fig. 4a shows characteristic cyclic voltammograms of the various $La_xCa_{1-x}MnO_3$ nanostructures supported on a meso-

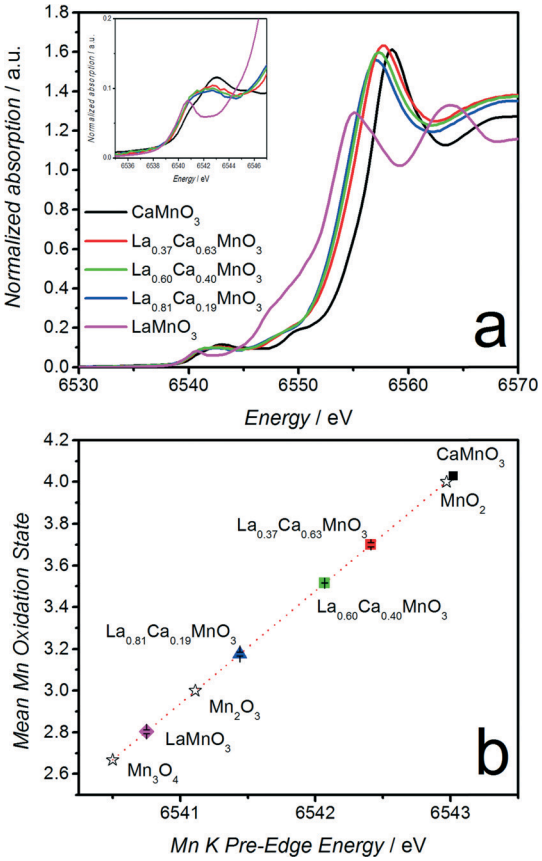

Fig. 3 *Ex situ* XANES spectra at the Mn K-edge for various compositions of the $La_xCa_{1-x}MnO_3$ samples (a). The inset in (a) shows the Mn K pre-edge features used for quantifying the mean oxidation state. Mean Mn oxidation state as a function of the pre-edge position for the standard Mn_3O_4, Mn_2O_3 and MnO_2 compounds, as well as for the various $La_xCa_{1-x}MnO_3$ samples (b). The dashed line in (b) is a linear fit to the positions of the standard compounds to yield a calibration curve and the points for the various $La_xCa_{1-x}MnO_3$ samples have been placed on the line according to the measured position of the Mn K pre-edge feature.

porous carbon layer (Vulcan) in argon-saturated 0.1 M KOH solution at 0.010 V s^{-1}. The oxide loading was kept constant at 250 μg cm^{-2} in all experiments. The faradaic charges associated with the anodic and cathodic peaks are very similar, and the responses remain stable in this potential range. These results suggest that the stability of these materials is not significantly compromised within the timescale of these experiments. Investigations carried out over a wide potential range revealed that the stability of the oxide appears to be compromised at potentials above 1.7 V. $LaMnO_3$ features two cathodic reduction peaks located at 0.90 and 0.50 V, which have been described in terms of the formation of a partially reduced state, prior to the reduction of Mn^{2+}.[11,16,44,45] The voltammogram of $CaMnO_3$ is characterised by a broad reduction peak centred at 0.80 V, ascribed to the reduction of Mn^{4+} to Mn^{2+}.[44,45] A small feature at ~0.5 V is also observed superimposed to the main broad voltammetric peak, which may suggest the presence of Mn^{3+}-like sites at the surface of $CaMnO_3$. A systematic increase in current with increasing

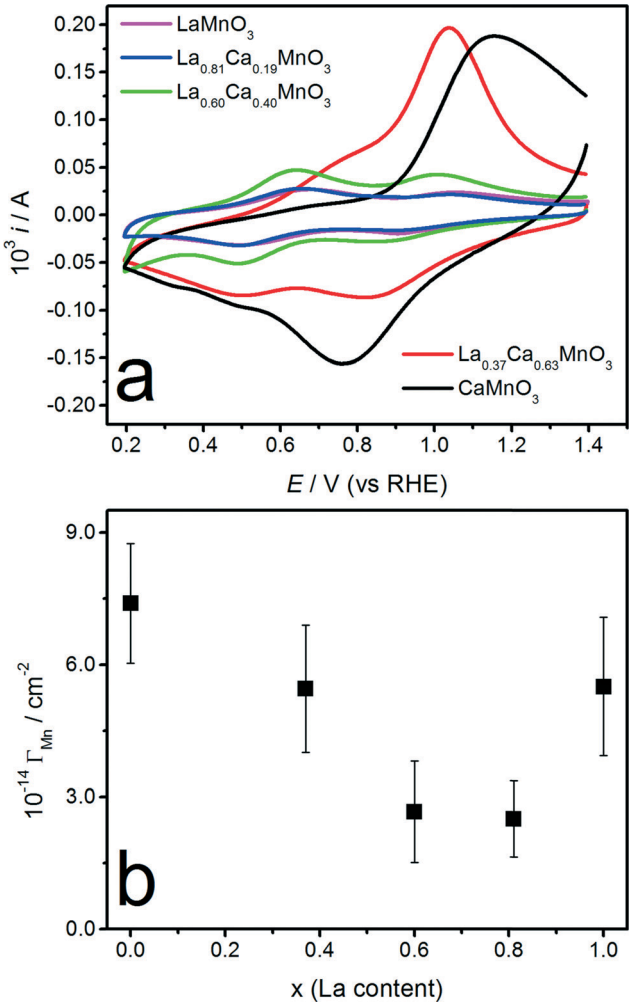

Fig. 4 Cyclic voltammograms of $CaMnO_3$, $La_{0.37}Ca_{0.63}MnO_3$, $La_{0.60}Ca_{0.40}MnO_3$, $La_{0.81}Ca_{0.19}MnO_3$ and $LaMnO_3$ nanoparticles supported on a mesoporous carbon electrode in Ar-saturated 0.1 M KOH solution at 0.010 V s^{-1} (a). The oxide content in each electrode was 250 μg cm^{-2}. As the Ca content increases, the intensity of the voltammetric features increases. The traces of $La_{0.81}Ca_{0.19}MnO_3$ and $LaMnO_3$ effectively overlap in this scale. Dependence of the effective Mn atomic surface density with La content (b). The number density of Mn sites was estimated from integrating the voltammetric responses. Details of these calculations are given in the ESI.†

Ca^{2+} content in the A-site is observed. This trend is also a reflection of the dependence of surface B-site depletion on the composition of the oxide. Although there are a number of interesting features in these voltammetric responses, which are still under investigation, we shall confine our analysis to the faradaic charges involved in the reduction of surface Mn sites. A recent study has also shown comparable voltammetric responses of various Mn oxides, including $LaMnO_3$, although the assignment of redox states is not compatible with our observations.[15]

The cyclic voltammograms in Fig. 4a allow estimating the mean Mn surface number density (Γ_{Mn}) for the various oxide compositions as shown in Fig. 4b.[16] The charge is obtained from integration of the voltammetric responses across the potential range in Fig. 4a, which reflect changes from the initial oxidation state of Mn sites to a Mn^{2+} state. It is important to note that the open circuit potential for all of the oxides is located at potentials slightly more positive than the onset of the reduction wave located around 0.9 V. Consequently, the effective redox state estimated from XANES can be considered as the initial state in the potential range investigated. Fig. S6† illustrates the background current correction used for integration of the voltammograms. Due to the large background current in the voltammetric responses, a self-consistent approach was implemented involving: (i) balancing the charges of oxidation and reduction features, and (ii) systematic variation of the background threshold. The error bars associated with the charge in Table S7† and Mn number density (Fig. 4b) include this systematic analysis of the background current. Table S7† summarises the values obtained from the integration of the voltammetric signals and the methodology used for estimating Γ_{Mn}, employing density values obtained from the XRD refinement and the mean particle size. It is rather remarkable that Γ_{Mn} (Fig. 4b) and the B/A-site ratio obtained from XPS (Fig. 2e) show a very similar composition dependence. This observation demonstrates that voltammetric analysis can provide useful information on the surface composition of these oxides. However, it should also be considered that the penetration depth of XPS (in the range of 6 nm) probes a larger portion of the oxide composition with respect to the electrochemical signal, which is sensitive to the oxide/electrolyte boundary.

Disk (i_{DISK}, bottom panel) and ring (i_{RING}, top panel) currents obtained at 1600 rpm and 0.010 V s^{-1} in an O_2-saturated 0.1 M KOH solution are contrasted in Fig. 5 for all of the carbon-supported oxides. The ORR onset potential is significantly more positive than that of the Vulcan support (*ca.* 0.7 V),[16] confirming that the reaction mainly takes place at the oxide particles at low overpotentials. Substantial peroxide detection at the ring electrode is not observed until 0.7 V, further indicating that ORR mainly occurs through a four-electron mechanism. The most positive onset potential is observed for $LaMnO_3$, while $CaMnO_3$ requires a higher overpotential to initiate the reaction. As illustrated in Fig. S7,† the shift in ORR onset potential appears to mirror the displacement in the first peak of Mn reduction. This observation is consistent with our previous studies linking the ORR kinetics with increasing electron density at the Mn site under operational conditions.[16]

The ring and disk current responses as a function of the rotation rate for $CaMnO_3$ are displayed in Fig. S8.† In Fig. S9,† it can be seen that the effective number of transferred electrons (n) and the hydrogen peroxide yield (% HO_2^-) are above 3.5 and below 25% for all of the perovskite nanostructures. The Koutecky–Levich plots in the range of 0.53 to 0.64 V (Fig. S10a–e†) are characterised by slopes consistent with the four-electron reduction process. From these plots, the kinetic current as a function of the applied potential can be extracted as shown in Fig. S10f.†

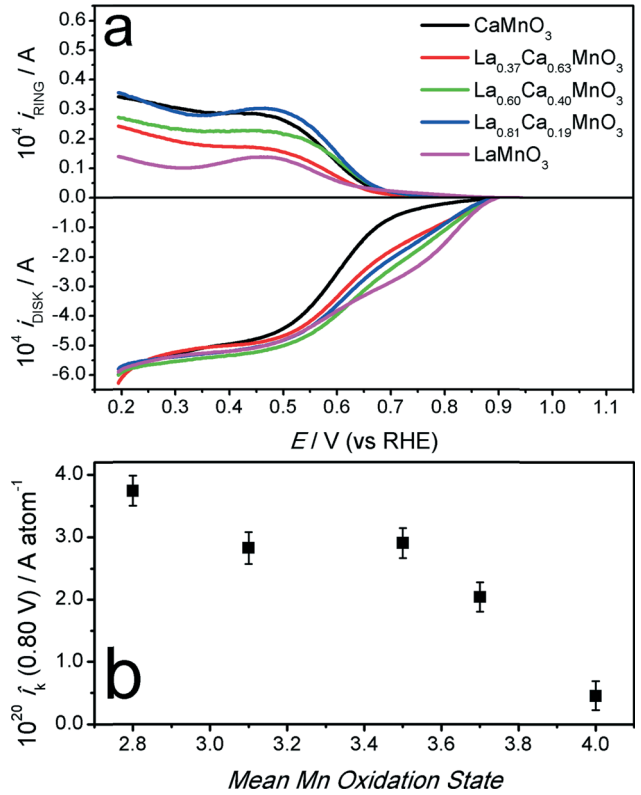

Fig. 5 RRDE responses of the various $La_xCa_{1-x}MnO_3$ nanoparticles supported on a thin mesoporous carbon layer at 1600 rpm in O_2-saturated 0.1 M KOH at 0.010 V s^{-1} (a). The Pt ring was held at a constant potential of 1.10 V. The oxide content in each electrode was 250 μg cm^{-2}. Kinetic current at 0.80 V *vs.* RHE normalised by the effective number of Mn atoms at the surface (b).

Fig. 5b displays the kinetic current at 0.80 V normalised by the effective number of surface Mn sites (Table S7†). For the first time, we can demonstrate a clear trend in the activity of surface Mn sites with the mean oxidation state. To put these values in the context of conventional benchmarking, Fig. S11† shows the normalisation of the kinetic current by catalyst mass and specific surface area. At first, the data show that these materials are among the most active reported for the ORR.[6] Interestingly, normalisation by these parameters leads to non-monotonic dependencies with La content. Consequently, we conclude that systematic analysis of catalyst performance as a function of the oxide composition requires explicit determination of the A-site surface segregation and oxygen vacancies (affecting the B-site oxidation state).

Finally, the physical principles responsible for the correlation between ORR catalytic performance and the oxidation state of the Mn site remain to be elucidated. From a simplistic phenomenological point of view, it could be postulated that higher electron density at the Mn-site leads to a higher capacity for O–O bond breaking. It should also be considered that the effective electron density of the surface Mn sites is affected not only by the valency of the A-site and oxygen vacancies, but crucially by the electrode potential. Although this description offers guiding principles for optimisation of Mn-based perovskites, the physical rationalisation of this observation requires complex theoretical modelling capable of including the effect of water.

3. Conclusion

The electrochemical activity of $La_xCa_{1-x}MnO_3$ towards the ORR reaction is strongly affected by the mean oxidation state of the Mn site, with the most active material featuring the highest electron density at potentials close to the reversible ORR potential. Detailed characterisation of the nanostructured materials employing quantitative XRD, XANES and XPS analysis allowed identification of their bulk and surface chemical composition, and the mean Mn oxidation state. Electrochemical studies in the absence of O_2 provided information on the number of surface active Mn sites. The ensemble of these results enabled the extraction of the characteristic kinetic current of the carbon-supported catalysts, taking into account complex parameters such as A-site segregation.

We strongly believe that any attempt to establish structure–reactivity relationships should carefully consider the complex surface chemistry of these oxides. Normalisation by the mass of the catalysts can provide useful information in terms of overall performance. However, this approach does not consider phenomena such as surface segregation, which is strongly dependent on the nature of the A-site and the oxide phase formation temperature. In this particular family of compounds, La^{3+} promotes the optimum oxidation state for Mn although the overall activity of the catalysts is somewhat compromised by the strong tendency of La^{3+} to segregate at the oxide surface in comparison to Ca^{2+}. Based on these observations, we can predict that promoting the highly electron-rich Mn site, crystallised at low temperatures, may lead to a substantial increase in the ORR activity.

Experimental section

Oxide nanoparticle synthesis

The preparation of phase-pure $La_xCa_{1-x}MnO_3$ nanoparticles is based on the ionic liquid/cellulose method.[16,46,47] The ionic precursor, an aqueous mixture of 0.1 M $La(NO_3)_3$, 0.1 M $Ca(NO_3)_2$ and 0.1 M $Mn(NO_3)_3$, was prepared in the desired stoichiometric ratio from the anhydrous salts (Sigma Aldrich). The ionic precursor (1 mL) was mixed with 1-ethyl-3-methylimidazolium acetate (1 mL) and heated at 80 °C for 3 hours to facilitate evaporation of water. Microcrystalline cellulose (100 mg, 10 wt%) was added yielding a smooth, homogeneous gel. The dehydrated precursor gel was calcined immediately after preparation under air for 2 hours at 700 °C. For $CaMnO_3$, a dwell temperature of 850 °C was required to achieve a crystalline structure.

X-ray diffraction and Rietveld refinement

X-ray diffraction (XRD) patterns were recorded using a Bruker AXS D8 Advance diffractometer with a θ–θ configuration,

using Cu Kα radiation (λ = 0.154 nm). Experiments were run between 10 and 90 degrees, using a step size of 0.02 degrees. The XRD patterns were refined by the Rietveld method using the FULLPROF program.[48,49] The following parameters were refined: scale factor, background coefficients, zero-point error and positional coordinates. The isotropic thermal factors for all the atoms were fixed to a standard value of 1 $Å^2$. In the pure La and Ca samples, no cation deficiency was detected and so the occupancy factors were fixed to 1. For the mixed composition samples, the occupancy factors for La and Ca were also refined.

Microscopy and photoemission spectroscopy

Transmission electron microscopy (TEM) and high-resolution TEM analysis were performed using a JEOL JEM-1400Plus and a JEOL JEM 2010, respectively. Samples for TEM were produced by placing 1 mL drops of the oxide particles dissolved in ethanol on a 3 mm diameter carbon-coated copper grid. Mean particle diameters were estimated from at least 100 nanoparticles per sample. X-ray Photoelectron Spectroscopy (XPS) was carried out in a custom-designed UHV system equipped with an EA 125 Omicron electron analyser, working at a base pressure of 10^{-9} mbar. Core level photoemission spectra (C 1s, Ca 2p, O 1s, Mn 2p and La 3d regions) were collected in normal emission at room temperature with a non-monochromatic Al K_α X-ray source (1486.7 eV) and using 0.1 eV steps, 0.5 s collection time and 20 eV pass energy. The binding energies (BEs) were referenced to the C 1s peak at 284.6 eV. The surface composition of the samples was obtained from the Ca 2p, Mn 2p and La 3d peak regions taking into account the corresponding sensitivity factors. Furthermore, photoemission data was also collected in normal emission at room temperature with a non-monochromatic Mg K_α X-ray source (1253.6 eV), in order to avoid the contribution of the La MNN Auger peak (854 eV with Al K_α) to the La 3d photoemission line. In this case, 0.2 eV steps, 0.5 s collection time and 50 eV pass energy were used.

X-ray absorption near-edge spectroscopy (XANES)

XANES spectra were recorded in transmission mode at the Mn K-edge (6539 eV), on beamline B18 at Diamond Light Source operating with a ring energy of 3 GeV and at a current of 300 mA. The monochromator comprises Si(311) crystals operating in Quick EXAFS mode. Calibration of the monochromator was carried out using a Mn foil. The samples were prepared as pellets (1.32 cm^2 pellet area) by mixing the ground sample with cellulose (~80 mg) to form a homogeneous mixture, and then compressed (~5 tons) using a pellet press. The amount of sample to prepare the pellet was calculated in order to obtain a manganese absorbance of 1. A total of three spectra were averaged for each sample. The data was analysed using the Athena program.[50] The spectra were aligned using the Mn foil response.

Electrochemistry

Electrochemical measurements were conducted in a three-electrode cell using a rotating ring-disk electrode (RRDE) fitted to an ALS rotation controller and connected to a CompactStat bipotentiostat (Ivium). The RRDE electrode consisted of a 4 mm glassy carbon disk surrounded by a Pt ring. The collection efficiency was experimentally determined to be 0.4. Hg/HgO (in 1 M NaOH, IJ Cambria) was used as the reference electrode. The potentials in this work have been converted in reference to a RHE. Measurements were carried out in 0.1 M KOH saturated with either purified Ar or O_2 (BOC). A thin-film catalyst layer was deposited on the glassy carbon electrode using a two-step drop-casting method with two different inks. An ink containing Vulcan XC-72 carbon and Na^+-exchanged Nafion® (5 wt%, Sigma-Aldrich) is deposited on the glassy carbon disk, followed by deposition of an aqueous suspension of the oxide. The final loading in the catalyst layer for each electrode was controlled at 250 μg_{OXIDE} cm^{-2}, 50 μg_{VULCAN} cm^{-2} and 50 μg_{NAFION} cm^{-2} (per geometric surface area of the electrode).

Further details of the crystal structure investigation(s) may be obtained from Fachinformationszentrum Karlsruhe, 76344 Eggenstein-Leopoldshafen (Germany), on quoting the depository numbers CSD 431077, 431082, 431086, 431090 and 431091.

Acknowledgements

VC gratefully acknowledges the UK National Academy and the Royal Society for the support through the Newton International Fellows program. VC, ED, AER, AA, DK and DJF are grateful for the resources and support provided by the UK Catalysis Hub Consortium (EPSRC grants EP/K014706/1 and EP/K014714/1). TEM studies were carried out at the University of Bristol Chemistry Imaging Facility with equipment funded by UoB and EPSRC (EP/K035746/1 and EP/M028216/1). The authors wish to acknowledge Diamond Light Source for provision of beamtime (SP10306).

References

1 J. Wu and H. Yang, *Acc. Chem. Res.*, 2013, **46**, 1848–1857.
2 H. A. Gasteiger, S. S. Kocha, B. Sompalli and F. T. Wagner, *Appl. Catal., B*, 2005, **56**, 9–35.
3 A. Grimaud, W. T. Hong, Y. Shao-Horn and J. M. Tarascon, *Nat. Mater.*, 2016, **15**, 121–126.
4 D. Chen, C. Chen, Z. M. Baiyee, Z. Shao and F. Ciucci, *Chem. Rev.*, 2015, **115**, 9869–9921.
5 F. Jaouen, E. Proietti, M. Lefevre, R. Chenitz, J.-P. Dodelet, G. Wu, H. T. Chung, C. M. Johnston and P. Zelenay, *Energy Environ. Sci.*, 2011, **4**, 114–130.
6 Z. Chen, D. Higgins, A. Yu, L. Zhang and J. Zhang, *Energy Environ. Sci.*, 2011, **4**, 3167–3192.
7 J. Suntivich, H. A. Gasteiger, N. Yabuuchi, H. Nakanishi, J. B. Goodenough and Y. Shao-Horn, *Nat. Chem.*, 2011, **3**, 647–651.

8 F. Calle-Vallejo, N. G. Inoglu, H.-Y. Su, J. I. Martinez, I. C. Man, M. T. M. Koper, J. R. Kitchin and J. Rossmeisl, *Chem. Sci.*, 2013, **4**, 1245–1249.
9 E. M. Fernández, P. G. Moses, A. Toftelund, H. A. Hansen, J. I. Martínez, F. Abild-Pedersen, J. Kleis, B. Hinnemann, J. Rossmeisl, T. Bligaard and J. K. Nørskov, *Angew. Chem., Int. Ed.*, 2008, **47**, 4683–4686.
10 W. T. Hong, M. Risch, K. A. Stoerzinger, A. Grimaud, J. Suntivich and Y. Shao-Horn, *Energy Environ. Sci.*, 2015, **8**, 1404–1427.
11 W. G. Hardin, J. T. Mefford, D. A. Slanac, B. B. Patel, X. Wang, S. Dai, X. Zhao, R. S. Ruoff, K. P. Johnston and K. J. Stevenson, *Chem. Mater.*, 2014, **26**, 3368–3376.
12 W. Lee, J. W. Han, Y. Chen, Z. Cai and B. Yildiz, *J. Am. Chem. Soc.*, 2013, **135**, 7909–7925.
13 J. Druce, H. Tellez, M. Burriel, M. D. Sharp, L. J. Fawcett, S. N. Cook, D. S. McPhail, T. Ishihara, H. H. Brongersma and J. A. Kilner, *Energy Environ. Sci.*, 2014, **7**, 3593–3599.
14 G. Kéranguéven, S. Royer and E. Savinova, *Electrochem. Commun.*, 2015, **50**, 28–31.
15 A. S. Ryabova, F. S. Napolskiy, T. Poux, S. Y. Istomin, A. Bonnefont, D. M. Antipin, A. Y. Baranchikov, E. E. Levin, A. M. Abakumov, G. Kéranguéven, E. V. Antipov, G. A. Tsirlina and E. R. Savinova, *Electrochim. Acta*, 2016, **187**, 161–172.
16 V. Celorrio, E. Dann, L. Calvillo, D. J. Morgan, S. R. Hall and D. J. Fermin, *ChemElectroChem*, 2016, **3**, 283–291.
17 T. Poux, A. Bonnefont, G. Kéranguéven, G. A. Tsirlina and E. R. Savinova, *ChemPhysChem*, 2014, **15**, 2108–2120.
18 K. A. Stoerzinger, M. Risch, B. Han and Y. Shao-Horn, *ACS Catal.*, 2015, **5**, 6021–6031.
19 M. Yuasa, N. Yamazoe and K. Shimanoe, *J. Electrochem. Soc.*, 2011, **158**, A411–A416.
20 M. Yuasa, N. Tachibana and K. Shimanoe, *Chem. Mater.*, 2013, **25**, 3072–3079.
21 M. Yuasa, K. Shimanoe, Y. Teraoka and N. Yamazoe, *Electrochem. Solid-State Lett.*, 2011, **14**, A67–A69.
22 J. Tulloch and S. W. Donne, *J. Power Sources*, 2009, **188**, 359–366.
23 K. A. Stoerzinger, W. Lü, C. Li, Ariando, T. Venkatesan and Y. Shao-Horn, *J. Phys. Chem. Lett.*, 2015, **6**, 1435–1440.
24 K. A. Stoerzinger, M. Risch, J. Suntivich, W. M. Lu, J. Zhou, M. D. Biegalski, H. M. Christen, Ariando, T. Venkatesan and Y. Shao-Horn, *Energy Environ. Sci.*, 2013, **6**, 1582–1588.
25 J. Du, T. Zhang, F. Cheng, W. Chu, Z. Wu and J. Chen, *Inorg. Chem.*, 2014, **53**, 9106–9114.
26 Z. Cai, M. Kubicek, J. Fleig and B. Yildiz, *Chem. Mater.*, 2012, **24**, 1116–1127.
27 R. Shannon, *Acta Crystallogr., Sect. A: Cryst. Phys., Diffr., Theor. Gen. Crystallogr.*, 1976, **32**, 751–767.
28 J. Rodríguez-Carvajal, M. Hennion, F. Moussa, A. H. Moudden, L. Pinsard and A. Revcolevschi, *Phys. Rev. B: Condens. Matter Mater. Phys.*, 1998, **57**, R3189–R3192.
29 C. N. Borca, S. Canulescu, F. Loviat, T. Lippert, D. Grolimund, M. Döbeli, J. Wambach and A. Wokaun, *Appl. Surf. Sci.*, 2007, **254**, 1352–1355.
30 R. Dudric, A. Vladescu, V. Rednic, M. Neumann, I. G. Deac and R. Tetean, *J. Mol. Struct.*, 2014, **1073**, 66–70.
31 N. H. Batis, P. Delichere and H. Batis, *Appl. Catal., A*, 2005, **282**, 173–180.
32 D. Mierwaldt, S. Mildner, R. Arrigo, A. Knop-Gericke, E. Franke, A. Blumenstein, J. Hoffmann and C. Jooss, *Catalysts*, 2014, **4**, 129–145.
33 N. Gunasekaran, S. Rajadurai, J. J. Carberry, N. Bakshi and C. B. Alcock, *Solid State Ionics*, 1994, **73**, 289–295.
34 N. A. Merino, B. P. Barbero, P. Eloy and L. E. Cadús, *Appl. Surf. Sci.*, 2006, **253**, 1489–1493.
35 T. Jin and K. Lu, *J. Power Sources*, 2011, **196**, 8331–8339.
36 J. A. Kilner and M. Burriel, *Annu. Rev. Mater. Res.*, 2014, **44**, 365–393.
37 G. Subías, J. García, M. G. Proietti and J. Blasco, *Phys. Rev. B: Condens. Matter Mater. Phys.*, 1997, **56**, 8183–8191.
38 J. Garcia, G. Subias, V. Cuartero and J. Herrero-Martin, *J. Synchrotron Radiat.*, 2010, **17**, 386–392.
39 J. García, M. C. Sánchez, G. Subías and J. Blasco, *J. Phys.: Condens. Matter*, 2001, **13**, 3229.
40 E. A. Ahmad, G. Mallia, D. Kramer, V. Tileli, A. R. Kucernak and N. M. Harrison, *Phys. Rev. Lett.*, 2012, **108**, 259701.
41 A. Y. Ignatov, S. Khalid, R. Sujoy and N. Ali, *J. Synchrotron Radiat.*, 2001, **8**, 898–900.
42 J. Chaboy, *J. Synchrotron Radiat.*, 2009, **16**, 533–544.
43 M. Croft, D. Sills, M. Greenblatt, C. Lee, S. W. Cheong, K. V. Ramanujachary and D. Tran, *Phys. Rev. B: Condens. Matter Mater. Phys.*, 1997, **55**, 8726–8732.
44 H.-Y. Su, Y. Gorlin, I. C. Man, F. Calle-Vallejo, J. K. Norskov, T. F. Jaramillo and J. Rossmeisl, *Phys. Chem. Chem. Phys.*, 2012, **14**, 14010–14022.
45 M. Wiechen, H.-M. Berends and P. Kurz, *Dalton Trans.*, 2012, **41**, 21–31.
46 V. Celorrio, K. Bradley, O. J. Weber, S. R. Hall and D. J. Fermín, *ChemElectroChem*, 2014, **1**, 1667–1671.
47 D. C. Green, S. Glatzel, A. M. Collins, A. J. Patil and S. R. Hall, *Adv. Mater.*, 2012, **24**, 5767–5772.
48 H. Rietveld, *J. Appl. Crystallogr.*, 1969, **2**, 65–71.
49 J. Rodríguez-Carvajal, *Phys. B*, 1993, **192**, 55–69.
50 B. Ravel and M. Newville, *J. Synchrotron Radiat.*, 2005, **12**, 537–541.

